Atomically thin superfluid and solid phases for atoms on strained graphene

Sang Wook Kim,[1] Mohamed Marwan Elsayed,[1] Nathan S. Nichols,[2] Taras Lakoba,[3] Juan Vanegas,[1] Carlos Wexler,[4] Valeri N. Kotov,[1] and Adrian Del Maestro[5,6,7]

[1]*Department of Physics, University of Vermont, Burlington, Vermont 05405, USA*
[2]*Argonne Leadership Computing Facility, Argonne National Laboratory, Argonne, Illinois 60439, USA*
[3]*Department of Mathematics & Statistics, University of Vermont, Burlington, Vermont 05405, USA*
[4]*Department of Physics and Astronomy, University of Missouri, Columbia, Missouri 65211, USA*
[5]*Department of Physics and Astronomy, University of Tennessee, Knoxville, Tennessee 37996, USA*
[6]*Min H. Kao Department of Electrical Engineering and Computer Science, University of Tennessee, Knoxville, Tennessee 37996, USA*
[7]*Institute for Advanced Materials & Manufacturing, University of Tennessee, Knoxville, Tennessee 37920, USA*

(Received 1 February 2023; accepted 17 January 2024; published 20 February 2024; corrected 1 March 2024)

Atoms deposited on atomically thin substrates are a playground for exotic quantum many-body physics due to the highly tunable, atomic-scale nature of the interaction potentials. The ability to engineer strong interparticle interactions can lead to the emergence of collective states of matter, not possible in the context of dilute atomic gases confined in optical lattices. While it is known that the first layer of adsorbed helium on graphene is permanently locked into a solid phase, we motivate, with a physically intuitive mean-field calculation, and confirm, with quantum Monte Carlo simulations, that simple isotropic graphene lattice expansion unlocks a large variety of two-dimensional ordered commensurate, incommensurate, cluster atomic solid, and superfluid states for adsorbed atoms. It is especially significant that an atomically thin superfluid phase of matter emerges under experimentally feasible strain values, with potentially supersolid phases in close proximity on the phase diagram.

DOI: 10.1103/PhysRevB.109.064512

I. INTRODUCTION

Seeking to understand the behavior of strongly interacting electrons in quantum materials, where the Hamiltonian may be known from first principles but it is not possible to fully predict all emergent behaviors, has led to a fruitful program of quantum simulation [1], where analogous systems are constructed from well-understood and controllable constituents. Promising examples include the study of atoms confined in optical lattice potentials [2–4], electrons in two-dimensional (2D) materials [5,6], Rydberg arrays [7], and superconducting circuits [8]. These approaches can realize lattice Hamiltonians on mesoscopic scales, or at low densities; however, generating strong interactions at the atomic scale remains a challenge. A promising route is the construction of synthetic matter where atoms are adsorbed onto a physical substrate with [9] or without [10,11] chemical bonding.

Here we consider the latter case of bosonic ^{4}He atoms adsorbed on graphene, where both atom-atom and atom-substrate interactions are driven by van der Waals (VDW) dispersion forces. This is an ideal platform to study many-body phenomena, and thick multilayer adsorbed ^{4}He films have been a subject of considerable interest for over half a century. They have informed our understanding of criticality, including the role of the healing length [12] and the universal jump of the superfluid density at the Kosterlitz-Thouless (KT) transition [13,14]. For a graphite substrate, the presence of strong adsorption sites forming a triangular lattice (the dual lattice of graphite hexagon centers) produces commensurate and incommensurate solid phases in the first layer of adsorbed ^{4}He, observable by anomalies in the heat capacity [15–18]. In the second and higher adsorbed layers, the ^{4}He atoms can form a superfluid phase at a temperature T_{KT} below the bulk T_λ, detectable via third sound or a frequency shift of the adsorbed mass with a torsional oscillator [19–21]. Further details on the coverage-temperature phase diagram have been obtained by numerical simulations exploiting different forms of the graphite-helium interaction [22–25]. While it has ultimately been understood that bulk helium does not exhibit a supersolid phase, one that simultaneously breaks translational and gauge symmetries [26], the existence of supersolidity in models of hard-core bosons on the triangular lattice [27] makes adsorbed helium on graphite a candidate system for realizing exotic phases. Recent experimental results provide some support for this scenario, arguing that while the first layer remains insulating, thick helium films may exhibit intertwined superfluid and density wave order [28–30].

The propensity for insulating behavior in the first layer can be understood as following from the magnitude of the corrugation potential ($\sim$30 K), that localizes atoms through an exponential suppression of tunneling between triangular lattice adsorption sites. It is thus natural to consider replacing the graphite substrate with graphene, providing the same triangular lattice, but with a 10% weaker potential. This has motivated a flurry of quantum Monte Carlo simulations at both zero and finite temperature predicting different (and sometimes contradictory) phase diagrams for the second and higher adsorbed layers of ^{4}He [31–37]. However, there is consensus that first adsorbed layer appears to remain stubbornly

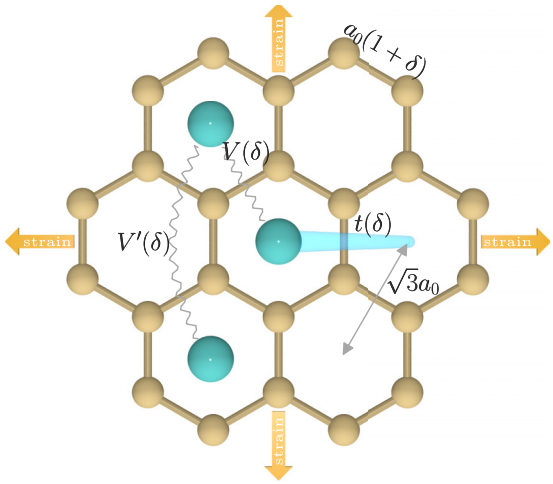

FIG. 1. Interactions between atoms adsorbed on graphene can be manipulated via mechanical biaxial strain. The parameters of a Bose-Hubbard Hamiltonian (hopping t, nearest-neighbor V, and next-nearest-neighbor V' interactions) can be strong functions of the strain δ; see Sec. III.

insulating, showing no evidence of quantum delocalization, and providing little motivation for expanded experimental searches.

In this paper, we show that an atomically thin superfluid phase of ^{4}He *can* be realized in this experimentally realizable system via a quantum phase transition tuned by the application of moderate (5%–15%) biaxial (isotropic) strain to the graphene membrane (see Fig. 1). This is possible due to the fact that graphene can be mechanically stretched along one [38,39], or multiple axes [40,41] to produce an increase in the carbon-carbon bond length a_0. Strain increases the distance between adsorbed ^{4}He atoms, and over this Å scale, the interactions between them can change from strong (hard-core) repulsion to weak VDW attraction [42]. Consequently, graphene's adsorption potential can be viewed as an "effective 2D lattice" for the ^{4}He atoms with a period on the scale of atomic interactions. This setup, with tunable interatomic interactions, is conceptually very difficult to achieve for dilute gases in optical lattices [2] which may allow multiple (soft-core) bosons per site, with a tunable kinetic energy via the strength of the lattice potential. ^{4}He on graphene can realize an effective 2D hard-core Bose-Hubbard model with strain-dependent nearest- (V) and next-nearest- (V') neighbor interactions [43]. In the remainder of this paper, we define the details of both the microscopic and effective model describing the adsorbed atoms in Sec. II and explore the effects of strain on the latter by mean field calculations in Sec. III. We then confirm the mean field picture with large-scale *ab initio* quantum Monte Carlo simulations of ^{4}He on strained graphene at low temperature in Sec. IV. We conclude in Sec. V that this system is a highly tunable (via mechanical strain and pressure and chemical potential) platform for the experimental exploration and discovery of strictly two-dimensional strongly interacting quantum phases of matter.

II. MODEL: HELIUM NEAR STRAINED GRAPHENE

^{4}He atoms of mass m_4 interacting with a strained suspended graphene membrane can be described by the microscopic many-body Hamiltonian

$$H = -\frac{\hbar^2}{2m_4}\sum_{i=1}^{N}\nabla_i^2 + \sum_{i=1}^{N}\mathcal{V}_{\hexagon}(\boldsymbol{r}_i;\delta) + \sum_{i<j}\mathcal{V}(\boldsymbol{r}_i-\boldsymbol{r}_j). \quad (1)$$

Here, $\mathcal{V}_{\hexagon}$ is the adsorption potential experienced by an atom at spatial position $\boldsymbol{r}_i = (x_i, y_i, z_i)$ with strain captured by $\delta \equiv a/a_0 - 1$, quantifying the increase of the carbon-carbon distance a with respect to $a_0 \simeq 1.42$ Å; see next paragraph for more details. The interaction between ^{4}He atoms $\mathcal{V}$ is known to high precision [42,44]. In what follows we set the Boltzmann constant $k_B = 1$ and measure all energies in units of K.

We consider a strained graphene membrane that is frozen in place at $z = 0$ with lattice ($\boldsymbol{a}$) and basis ($\boldsymbol{b}$) vectors:

$$\boldsymbol{a}_1(\delta) = \frac{a_0(1+\delta)}{2}(\sqrt{3}, 3), \quad \boldsymbol{b}_1(\delta) = \frac{a_0(1+\delta)}{2}(\sqrt{3}, 1),$$
$$\boldsymbol{a}_2(\delta) = \frac{a_0(1+\delta)}{2}(-\sqrt{3}, 3), \quad \boldsymbol{b}_2(\delta) = a_0(1+\delta)(0, 1). \quad (2)$$

The resulting empirical interaction potential $\mathcal{V}_{\hexagon}$ between ^{4}He and the strained graphene is computed by assuming a superposition of isotropic 6–12 Lennard-Jones potentials between carbon and helium [45]:

$$\mathcal{V}_{\hexagon}(\boldsymbol{r}_i) = \frac{8\pi\varepsilon(\delta)\sigma^2(\delta)}{3\sqrt{3}a_0^2(1+\delta)^2}\left\{\left[\frac{2}{5}\left(\frac{\sigma(\delta)}{z_i}\right)^{10} - \left(\frac{\sigma(\delta)}{z_i}\right)^4\right]\right.$$
$$\left. + \sum_{\boldsymbol{g}\neq 0}\sum_{\ell=1}^{2} e^{i\boldsymbol{g}(\delta)\cdot[\mathbf{r}_i - \boldsymbol{b}_\ell(\delta)]}\left[\frac{1}{60}\left(\frac{g(\delta)\sigma(\delta)^2}{2z_i}\right)^5 K_5[g(\delta)z_i] - \left(\frac{g(\delta)\sigma(\delta)^2}{2z_i}\right)^2 K_2[g(\delta)z_i]\right]\right\}, \quad (3)$$

where $\sigma(\delta)$ and $\varepsilon(\delta)$ are strain-dependent Lennard-Jones parameters that have been computed via the method described in Ref. [46] with values and tabulated potentials (up to $\delta = 0.3$) available online [47]. In Eq. (3), $\mathbf{r}_i = (x_i, y_i)$ are the coordinates of a ^{4}He atom in the xy plane, and $\boldsymbol{g}(\delta) = n_1\boldsymbol{G}_1(\delta) + n_2\boldsymbol{G}_2(\delta)$ are the reciprocal lattice vectors with magnitude $g(\delta) \equiv |\boldsymbol{g}(\delta)|$, where $n_1, n_2 \in \mathbb{Z}$,

$$\boldsymbol{G}_1(\delta) = \frac{2\pi}{3a_0(1+\delta)}(\sqrt{3}, 1),$$
$$\boldsymbol{G}_2(\delta) = \frac{2\pi}{3a_0(1+\delta)}(-\sqrt{3}, 1) \quad (4)$$

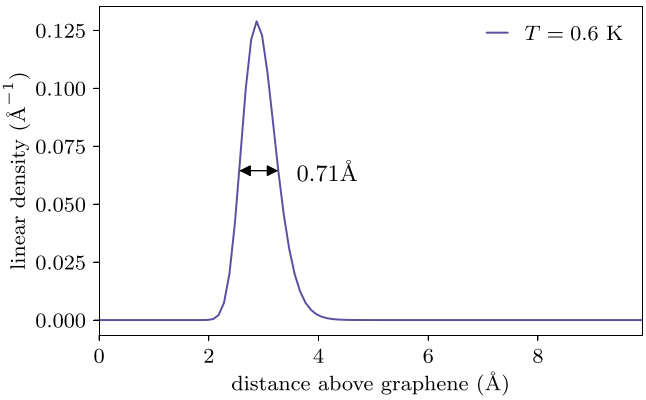

FIG. 2. The density of ^{4}He as a function of the distance above the graphene membrane at $\delta = 0.15$ for $\mu = -93$K at $T = 0.6$K. These parameters are shown, in Sec. IV, to correspond to the superfluid state of the adsorbed layer. The full width at half-maximum of 0.71 Å of the layer supports the effective 2D treatment within the Hartree-Fock and Bose-Hubbard pictures.

and K_n are modified Bessel functions which decay as $\exp(-gz_i)$ at large argument.

Numerical simulations of Eq. (1) with $\delta = 0$, for both graphite and graphene [22,23,31,34,35,43], are consistent with the respective experimentally observed phase diagrams for graphite [20,21]. As the pressure is increased from vacuum, there is a first-order transition where a single layer is adsorbed, forming a commensurate incompressible solid phase dubbed C1/3, where ^{4}He atoms are localized around every third of the strong binding sites. The C1/3 phase is stable over a range of chemical potentials [35,43,48] due to the strong repulsive interactions $\mathcal{V}(\sqrt{3}a_0) \approx 50$ K per atom when nearest-neighbor sites are occupied (see Fig. 1). As the pressure of the proximate helium gas is further increased, eventually other commensurate and incommensurate phases can be realized due to energetic compensation by the chemical potential, including those with proliferated domain walls [35].

In the unstrained graphene ($\delta = 0$), it is energetically favorable to form a second layer (and beyond) once the triangular lattice filling fraction reaches the value $n \simeq 0.6$. However, at all lower fillings for $\delta = 0$, the transverse width of the wave function of the adsorbed ^{4}He atoms remains on the atomic scale, and the problem can be viewed as quasi-2D [43]. For strained graphene ($\delta > 0$), quantum Monte Carlo simulations, reported in Sec. IV, show that for sufficiently large δ, this quasi-2D character of the first absorbed layer can persist for filling fractions up to $n = 1$. Figure 2 illustrates the 2D character by showing a typical example of the z cross section of the absorbed ^{4}He many-body wave function.

III. MOTIVATION: STRAIN TUNING AT THE MEAN-FIELD LEVEL

In this preliminary section we present mean-field arguments to motivate the physical picture of strain-tuned interaction that we later explore with quantum Monte Carlo simulations.

The strongly 2D character exhibited discussed in the previous section was recently exploited in Refs. [11,43] to demonstrate that the first adsorbed layer of ^{4}He on unstrained graphene ($\delta = 0$) is well characterized by an effective extended hard-core (infinite onsite repulsion) 2D Bose-Hubbard (BH) model on the triangular lattice. This represents the low-energy sector of the full microscopic Hamiltonian in Eq. (1) with effective parameters corresponding to hopping t and both nearest- (V) and next-nearest-neighbor (V') density-density interactions:

$$H_{\rm BH} = -t \sum_{\langle i,j \rangle} \left(b_i^\dagger b_j + b_j^\dagger b_i \right) + V \sum_{\langle i,j \rangle} n_i n_j + V' \sum_{\langle\langle i,j \rangle\rangle} n_i n_j - \mu \sum_i n_i. \tag{5}$$

Here $b_i^\dagger$ (b_i) creates (annihilates) a hard-core ^{4}He atom on site i of the triangular lattice (center of a graphene hexagon) and $n_i = b_i^\dagger b_i$ measures the number of atoms per site, with $[b_i, b_j^\dagger] = \delta_{ij}$. Subscripts $\langle i, j \rangle$ and $\langle\langle i, j \rangle\rangle$ indicate nearest and next-nearest neighbors, respectively. The chemical potential μ can be tuned to change the average filling fraction $n = \langle n_i \rangle$.

For ^{4}He on unstrained graphene, it is known from many-body as well as first-principle *ab initio* methods [43] that V is strongly repulsive, originating from the overlap of adsorbed localized particle wave functions on the scale of the lattice spacing, while V' is much weaker and attractive, due to the VDW tail, with the ratio $V/|V'| \simeq 30$. The phase diagram of Eq. (5) can be computed at the mean-field level [49] (see Appendix A for more details), and it exhibits well-known insulating phases at commensurate filling fractions $n = \frac{1}{3}, \frac{2}{3}, 1$, as well as a superfluid and supersolid phase, as a function of the chemical potential μ and hopping t as shown in Fig. 3(a). For the purposes of understanding the phase diagram, it is useful to plot things in terms of related dimensionless quantities. The ground state of ^{4}He on unstrained graphene at fixed μ above the first-order transition from vacuum is indicated by a cross ($\times$), explaining the stability of the aforementioned C1/3 phase at $n = \frac{1}{3}$.

A key observation from Fig. 3, which motivates this study, is as follows. While the microscopic interaction $\mathcal{V}$ in Eq. (1) is fixed, the effective ones in Eq. (5) experienced by adsorbed atoms are not, and instead are determined by wave-function overlap (see Ref. [43] and Appendix B) and can thus be modified through strain. As the carbon atoms are moved further apart, V and V' will be modified, leading to qualitative changes in the mean-field phase diagram as the ratio $V/|V'|$ is altered. Namely, as will be justified below, we expect this ratio to decrease and eventually change sign. Therefore, in Figs. 3(b) and 3(c) we show modified mean-field phase diagrams computed for $V/|V'| = 1$ and -1, respectively. In the former case, the location of $\times$ indicates that the ^{4}He monolayer is now in the superfluid phase, whereas in the latter case, one finds the monolayer in a strongly correlated $n = 1$ insulating phase. This latter phase is due to the adsorbed atoms becoming far enough apart that their dominant effective interaction (V) is due to the attractive VDW tail of the microscopic interaction $\mathcal{V}$.

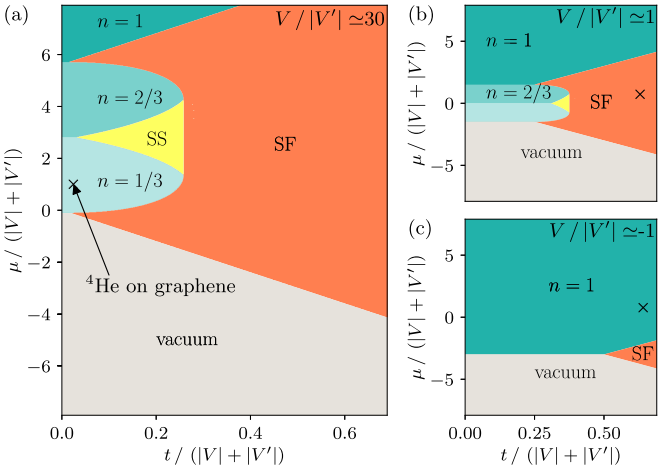

FIG. 3. (a) Mean-field phase diagram as a function of dimensionless chemical potential μ and hopping t for hard-core bosons on the 2D triangular lattice with the ratio of nearest- to next-nearest-neighbor interactions $V/|V'| \simeq 30$ (the physically realized value for $\delta = 0$). The ground state of the ^{4}He adsorbed layer (with physical parameters identified in Ref. [43]), is indicated by a $\times$ symbol at fixed μ. Lobes with crystalline phases appear at filling fractions $n = \frac{1}{3}, \frac{2}{3}$, and 1 as μ is increased for small t, and a superfluid phase (SF) is stable for larger t. (b), (c) show modified mean-field phase diagrams for $V/|V'| \simeq 1$ and $V/|V'| \simeq -1$, respectively, where the $\times$ symbol indicates the proposed phase for ^{4}He on strained graphene.

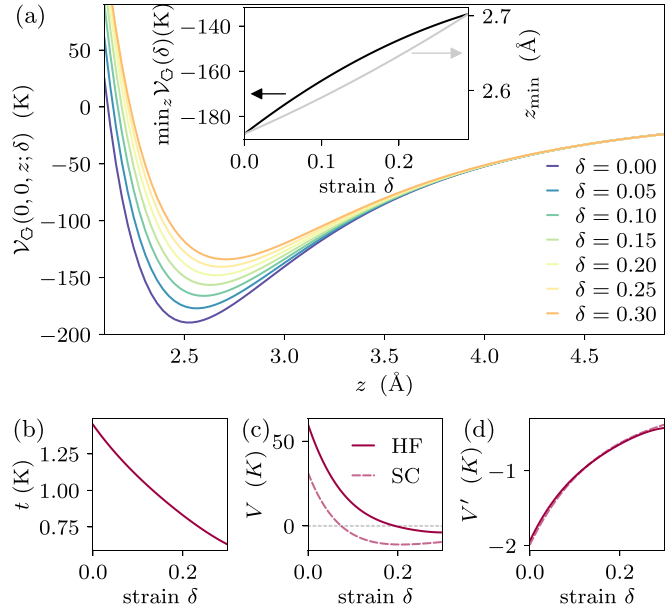

FIG. 4. (a) The helium-graphene adsorption potential $\mathcal{V}_{\hexagon}$ in Eq. (1) as a function of the height z of an atom above a graphene adsorption site for different values of strain δ. The inset quantifies how strain reduces the binding energy per atom (left axis) and shifts the location of the minimum, $z_{\min}$, (right axis) further from the membrane. (b)–(d) demonstrate the effects of strain on the effective 2D Bose-Hubbard model parameters t, V, and V' as computed via Hartree-Fock (HF); see Appendix B. Dashed lines in (c) and (d) correspond to the semiclassical (SC) predictions for the interaction parameters computed from $\mathcal{V}$ as $V_{\rm SC} \equiv \mathcal{V}[\sqrt{3}(1+\delta)a_0]$ and $V'_{\rm SC} \equiv \mathcal{V}[3(1+\delta)a_0]$; this approximation ignores the extended character of ^{4}He atoms' wave functions.

To confirm the above expectations about the ratio $V/|V'|$ as the lattice is isotropically expanded, we analyze the strain dependence of the microscopic adsorption potential $\mathcal{V}_{\hexagon}$ and resulting effective parameters of the 2D Bose-Hubbard model in Fig. 4. Figure 4(a) shows that for a single ^{4}He atom at height z above the center of a graphene hexagon, as strain is increased, the adsorption potential becomes less attractive, with a minimum that softens by 30% from -188 K for $\delta = 0$ to -134 K for $\delta = 0.3$. The location of the adsorbed 2D layer, expected to occur near this minimum $z_{\min}$, moves further from the sheet by 7% (2.5 Å $\rightarrow$ 2.7 Å). Thus, the increase of $z_{\min}$ is correlated with a decrease of the barrier height between lattice sites experienced by adsorbed atoms due to $\mathcal{V}_{\hexagon}$, and may cause a propensity for enhanced delocalization for $\delta > 0$. These changes in the microscopic adsorption potential are reflected in the effective parameters of the BH model shown in Figs. 4(b)–4(d). Parameters t, V, and V' are computed via Hartree-Fock theory from the average interaction energy at the nearest- and next-nearest-neighbor level determined from the self-consistent adsorbed wave functions; see Appendix B. They are compared with semiclassical (SC) predictions $V_{\rm SC} \equiv \mathcal{V}[\sqrt{3}(1+\delta)a_0]$ and $V'_{\rm SC} \equiv \mathcal{V}[3(1+\delta)a_0]$ computed directly from the ^{4}He-^{4}He interaction potential. As can be seen in Fig. 4(c), V experiences a drastic reduction as δ is increased, with strong wave-function renormalization effects, ultimately vanishing near 19% strain, and becoming attractive for $\delta > 0.2$. As V' is controlled by the VDW tail of $\mathcal{V}$, which already includes quantum effects at this scale, there is nearly perfect agreement between the semiclassical and the Hartree-Fock calculation. While the hopping t decreases by 50% due to the lattice expansion, this effect is dwarfed by the decrease of the normalization factor $(|V| + |V'|)$, which controls the mean-field phase diagram presented in Fig. 3 and ultimately pushes the adsorbed ^{4}He atoms into an energetic regime which can support superfluidity.

IV. RESULTS: COMPETING QUANTUM PHASES AND SUPERFLUID PHASE DIAGRAM VIA QUANTUM MONTE CARLO

To validate these predictions, and generate an experimentally relevant phase diagram, we have performed stochastically exact *ab initio* quantum Monte Carlo simulations of the full microscopic Hamiltonian in Eq. (1) for temperatures below $T_\lambda \simeq 2.17$ K. The details of our simulations, based on the Feynman path-integral formalism [50], are included in Appendix C, along with a description of how finite-size graphene simulations for cells with dimension $L_x \times L_y$ were extrapolated to the thermodynamic limit. The Monte Carlo code [51], unprocessed simulation data [52], and processed data and scripts [53] are readily available and can be utilized to reproduce all the figures presented in this paper.

For each value of strain between $0 \leqslant \delta \leqslant 0.30$ and for temperatures down to $T = 0.5$ K we perform a grand canonical Monte Carlo simulation as a function of chemical potential μ for system sizes corresponding to $N_{\hexagon} = 16, 36, 64, 90, 144$

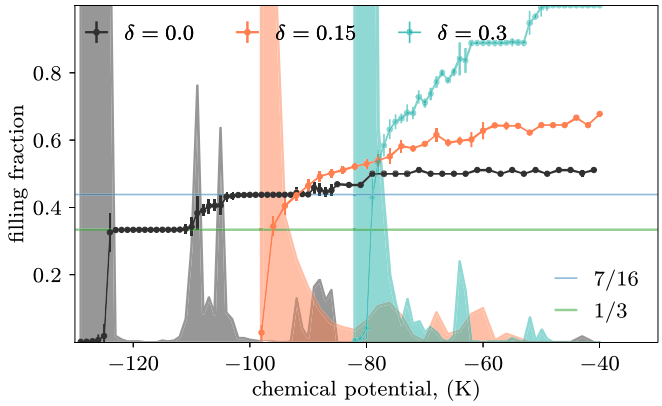

FIG. 5. Adsorption isotherms for ^{4}He on strained graphene. Points are quantum Monte Carlo results for the filling fraction $n = \langle N\rangle/N_{\hexagon}$ as a function of chemical potential μ for three values of strain at $T = 1.0$ K and $N_{\hexagon} = 90$. The filled region in the background corresponds to the normalized compressibility $\kappa \propto \langle (N - \langle N\rangle)^2\rangle$. Plateaus in the adsorption curves indicate incompressible solid phases, which may exist at commensurate filling fractions (indicated by horizontal lines at $n = \frac{1}{3}$ and $\frac{7}{16}$). A state with unit filling ($n = 1$) is only possible at high strains (e.g., $\delta = 0.3$ shown here) where the distance between triangular lattice adsorption sites has been stretched to a regime where the interactions between helium atoms become attractive. For $\delta = 0.15$, the qualitatively different onset behavior (characterized by the continuous increase in density and high compressibility) corresponds to the superfluid region of the phase diagram described in Fig. 6. Error bars represent standard statistical uncertainties from quantum Monte Carlo sampling.

strong adsorption sites. For each system size, temperature, and strain, we measure an adsorption isotherm $n(\delta)$ vs μ such as the ones for $\delta = 0.0, 0.15, 0.30$ shown in Fig. 5 at $T = 1$ K. For $\delta = 0$, as μ is increased, we find commensurate solid phases with filling fractions $n = \frac{1}{3}$ and $\frac{7}{16}$, that have been observed in previous simulations of unstrained graphene [35] and experiments with graphite substrates [18]. The $n = \frac{7}{16}$ solid is not realized in the BH lattice model, and is only energetically favorable in the presence of a smooth corrugation potential $\mathcal{V}_{\hexagon}$ as exists in the microscopic Hamiltonian in Eq. (1). The shaded background region shows the associated compressibility $\kappa \propto \langle N^2\rangle - \langle N\rangle^2$ in arbitrary units, where large values correspond to the first-order transition out of the vacuum, or to the transition between different commensurate (or incommensurate) solid phases. As the strain is increased, the initial adsorption transition out of the vacuum is pushed to larger (less negative) values of μ, consistent with the softening of the adsorption potential shown in Fig. 4. For $\delta = 0.15$, we observe a strong qualitative difference with the $\delta = 0$ case, as the onset of the first layer occurs over a wide range of chemical potentials indicated by a large band of finite compressibility. This behavior persists for the extreme value of $\delta = 0.3$, where we also observe new commensurate phases with large n appearing for $\mu \gtrsim -60$ K.

Putting all of these quantum Monte Carlo isotherms together, we can construct the low-temperature μ-δ phase diagram, shown in Fig. 6, that captures the strain dependence of the phases and phase transitions of the adsorbed helium monolayer. This phase diagram represents the main result of this work.

For low values of strain (<5%), we observe analogous behavior to the strain-free case already seen in Fig. 5 above with a first-order adsorption transition out of the vacuum leading to a well-defined incompressible monolayer with commensurate $n = \frac{1}{3}$ filling, followed by $n = \frac{7}{16}$ and other incommensurate phases upon increasing μ.

At strain increases, the strong nearest-neighbor repulsion between adsorbed ^{4}He atoms is reduced as the C-C distance increases. Above 5% strain, we observe a transition from either a low-density compressible liquid or vacuum to a superfluid. For $0.05 \lesssim \delta \lesssim 0.12$, this transition occurs around $\mu \simeq -101$ K, indicated as a horizontal line in Fig. 6 [for more detailed information along this cut see Fig. 7(a)]. Here, superfluidity is quantified within the two-fluid picture where the total adsorbed density of atoms is broken into normal and superfluid parts with $\rho = \rho_n + \rho_s$, where $\rho = \langle N\rangle/(L_x L_y)$ with $\langle N\rangle$ being the average number of adsorbed ^{4}He atoms, L_x, L_y being the dimensions of the simulation box, and ρ_s the superfluid density computed via the winding of particle world lines [54]; see Appendix C for calculation details. While the superfluid region for $0.05 \lesssim \delta \lesssim 0.12$ persists in the thermodynamic limit, ρ_s develops an aspect ratio dependence, suggesting this region could be nonuniversal. For larger values of strain $\delta \gtrsim 0.12$, the extended superfluid region is more robust, extending up to ∼25% strain and over a range of μ.

The inset to the main panel of Fig. 6 shows the density $\rho(x, y)$ of adsorbed atoms in the superfluid phase and illustrates the qualitatively different nature of this state, as compared to the solids shown in the six halos surrounding the main panel. In the superfluid, the density is nonvanishing across all adsorption sites, i.e., there is complete delocalization of ^{4}He atoms. In contrast, for a similar filling fraction $n \sim 0.4$ in halo No. 2, corresponding to a solid $n = \frac{7}{16}$ phase, ^{4}He atoms are localized around some 40% of the sites, with particle smears corresponding to the tunneling between different equivalent ground states appearing in our ergodic simulations. Also, within the superfluid phase, there is some evidence of coexisting solid order, but further work remains to be done to confirm the existence of a supersolid phase induced by the strained graphene lattice potential.

At the highest values of strain $\delta \gtrsim 0.24$, superfluidity no longer appears for any value of μ, and instead we observe the direct transition out of the vacuum to high filling fraction phases. Due to lattice expansion, interactions between adsorbed ^{4}He atoms on strong binding sites have become attractive (see Fig. 4), which for large μ culminates in the $n = 1$ state (see halo No. 6) predicted in our mean-field analysis. More details on the superfluid phase can be obtained by taking horizontal and vertical cuts through Fig. 6 with the results shown in Fig. 7. For fixed $\mu/k_B = -101$ K, the finite-temperature strain phase diagram [Fig. 7(a)] shows the onset of a finite superfluid fraction near $\delta = 0.03$ and the transition to vacuum for $\delta > 0.13$. The critical temperature for the onset of superfluidity remains relatively constant near $T \approx 1$ K over the entire phase. Fixing strain at $\delta = 0.12$, Fig. 7(b) presents both the total filling fraction n and the superfluid fraction ρ_s/ρ as a function of chemical potential, with the maximal superfluid signal occurring for $n \simeq 0.4$ and $\mu \simeq -97$ K.

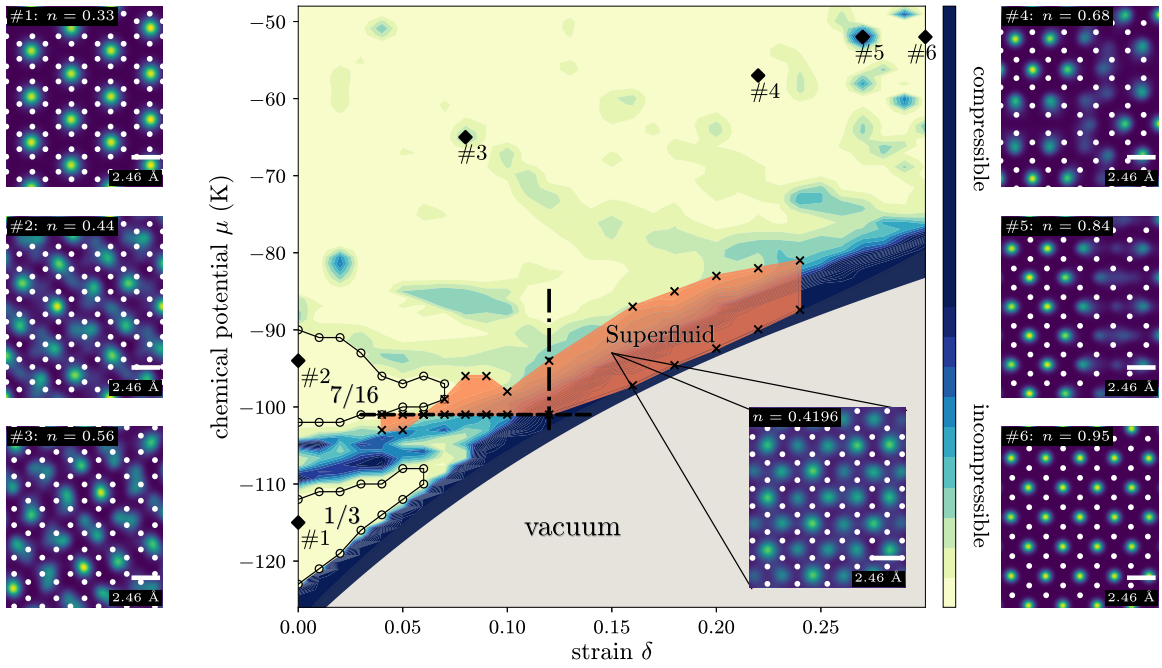

FIG. 6. Quantum Monte Carlo phase diagram (central panel) and adsorbed particle configurations (halos Nos. 1–6) as a function of chemical potential μ and isotropic strain $\delta = a/a_0 - 1$. The colored background of the main panel shows the compressibility of the adsorbed layer, with darker colors being more compressible. At small values of strain, large bounded regions indicate commensurate solid phases with $n = \frac{1}{3}$ and $\frac{7}{16}$ of adsorption sites filled. As strain is increased, a superfluid phase (SF, orange) emerges with a critical temperature above $T = 0.5$ K in the thermodynamic limit, with a boundary indicated by $\times$ symbols. The behavior of the superfluid and particle density along the indicated horizontal and vertical cuts is shown in Fig. 7. Subpanels (halos Nos. 1–6) show the average density $\rho(x, y)$ of adsorbed helium at different regions of the phase diagram (indicated by ⧫), detailing the particle configurations in both commensurate and incommensurate phases for $N_{\hexagon} = 48$ adsorption sites at $T = 1.0$ K. The filling fraction is indicated in each halo along with a scale bar highlighting the increase in the C-C separation. Small white dots indicate locations of carbon atoms. All are plotted on the same relative color scale [$\langle N \rangle = \int dx\, dy\, \rho(x, y)$] with dark blue indicating zero density and light greenish, the highest. At large strain, the unit filling phase predicted by the mean-field theory [see Fig. 3(c)] is observed in halo No. 6. It is important to note that the adsorbed density in the superfluid phase (bottom right inset of central panel) is qualitatively different from the density in the halos, exhibiting the delocalization of atoms between all adsorption sites, as discussed in the main text.

We close this section by noting that our fully microscopic and interacting phase diagram has a qualitative resemblance to the motivating mean-field predictions in Sec. III. This can be seen more clearly when recasting the axes in dimensionful units as shown in Fig. 8 in Appendix A.

V. DISCUSSION: PROSPECTS FOR MEASUREMENT

We have demonstrated through mean-field predictions for a low-energy effective lattice Bose-Hubbard model and confirmed by *ab initio* quantum simulations of a microscopic Hamiltonian, that isotropic biaxial strain applied to a graphene substrate can modify interactions between ^{4}He adatoms and lead to new atomically thin two-dimensional quantum phases and quantum transitions between them. It is thus natural to ask if this new superfluid phase could be realized in a real experiment. Graphene can withstand uniaxial mechanical strain of around 20% or more [39,55], and several-percent strain is now routinely realized [38,56,57]. Isotropic biaxial strain, as considered here, has been analyzed theoretically and also realized experimentally [39–41,58,59]. On a fundamental level, strain leads to substantial qualitative changes in electronic properties of the substrate, which can be calculated with great theoretical precision, and consequently generate predictions for measurable physical characteristics [39,60].

By combining well-known techniques to realize suspended graphene [61,62] (or other classes of two-dimensional materials, e.g., the dichalcogenide family $MoSe_2$, MoS_2, WSe_2, WS_2 [39,59,60]) with protocols that can simultaneously measure positional and superfluid responses of atoms adsorbed on flat [30,63,64] or curved [65] surfaces, the phase diagram in Fig. 6 could be experimentally explored.

In this regard, we stress that our quantum Monte Carlo phase diagram predicts the possibility of a monlayer superfluid phase of ^{4}He for values of isotropic strain as low as 4%, whereas recent experiments have achieved values of 2% for biaxial [41,58], and 4%–6% for uniaxial [56,59], strain. Thus, strain values required for observation of exotic phases of helium over 2D materials are on the cusp of experimental realization. Of course, such experiments are not performed under the "ideal" theoretical conditions assumed in our numerical modeling and could involve bending, proximity effects, strain asymmetry, etc, as well as not yet being performed at cryogenic temperatures. However, due to the rapid pace of technological developments in the field of two-dimensional materials, it is reasonable that such experiments are feasible in the near future. Such studies could be further motivated

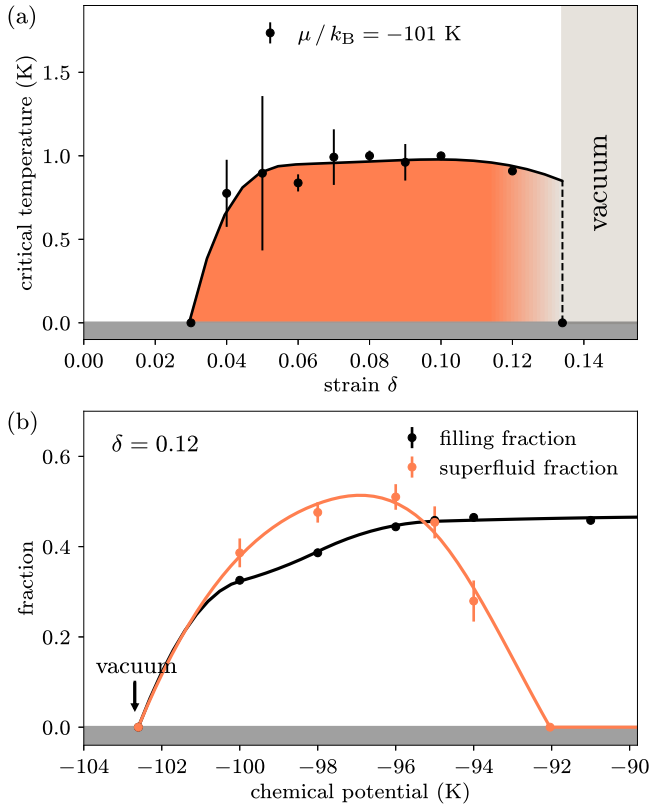

FIG. 7. (a) A horizontal cut at fixed chemical potential $\mu/k_B = -101$ K, indicated by the horizontal dashed line in Fig. 6, shows the finite-temperature onset of the superfluid phase as a function of strain. A nonvanishing superfluid fraction is measured up to the transition to the vacuum beyond $\delta = 0.13$. (b) The total particle filling fraction n and superfluid fraction ρ_s/ρ of the adsorbed atoms as a function of chemical potential μ at a fixed value of strain ($\delta = 0.12$) and temperature $T = 0.6$ K (the vertical dotted-dashed line in Fig. 6). In both panels, the error bars are computed as a combination of stochastic uncertainties from the Monte Carlo simulations and errors obtained from extrapolating to the thermodynamic limit. The smooth lines represent a guide to the eye.

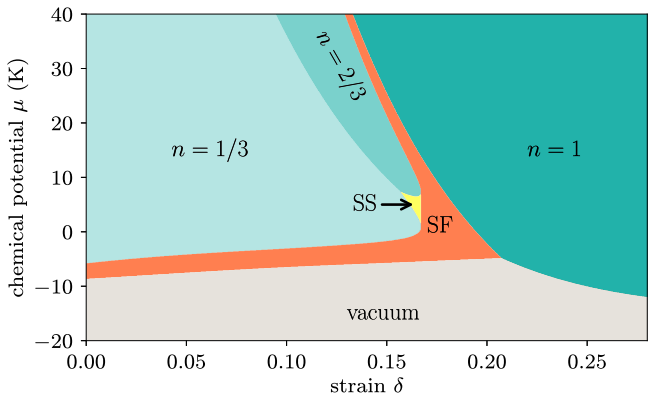

FIG. 8. Mean-field phase diagram of the extended 2D Bose-Hubbard model on the triangular lattice, presented in physical units of μ and δ. The diagram is based on the equations in Appendix A, with the strain dependence being introduced via that dependence of $t(\delta)$, $V(\delta)$, and $V'(\delta)$ from Fig. 4.

by Sec. IV, of the competition between superfluid and correlated solid orders throughout the phase diagram, which opens up the possibility of realizing an adsorbed supersolid phase induced by the graphene adsorption potential with broken gauge and lattice symmetries (as predicted by the mean-field theory in Figs. 3 and 8 and possibly already present in our quantum Monte Carlo results; see Fig. 6). Thus, the combination of strain-engineered substrates with a proximate quantum gas provides a new venue for the quantum simulation of tunable strongly interacting Hamiltonians via band structure modification.

ACKNOWLEDGMENTS

This work was supported by NASA Grant No. 80NSSC19M0143. Computational resources were provided by the NASA High-End Computing (HEC) Program through the NASA Advanced Supercomputing (NAS) Division at Ames Research Center. This research used resources of the Argonne Leadership Computing Facility, a U.S. Department of Energy (DOE) Office of Science user facility at Argonne National Laboratory and is based on research supported by the U.S. DOE Office of Science-Advanced Scientific Computing Research Program, under Contract No. DE-AC02-06CH11357.

APPENDIX A: MEAN-FIELD THEORY

Starting from the effective low-energy Bose-Hubbard Hamiltonian (5), the interaction terms can be decoupled for each lattice site i within the standard mean-field approach [49] leading to

$$H_{\mathrm{MF},i} = -6t[\psi(b_i + b_i^\dagger) - \psi^2] + 6(V + V')\left(\rho n_i - \frac{\rho^2}{2}\right) - \mu n_i, \tag{A1}$$

where we have introduced the condensate density $\langle b_i \rangle = \langle b_i^\dagger \rangle = \psi$ and the localized density $\langle n_i \rangle = \rho$. For an insulating state, $\psi = 0$. Diagonalizing in the basis of occupations numbers 0 and 1 of the triangular lattice gives the ground-state energy (per lattice site)

$$E = 6t\psi^2 + 3(V + V')\rho(1 - \rho) - \frac{\mu}{2} - \sqrt{\left(\frac{\mu - 6(V + V')\rho}{2}\right)^2 + (6t\psi)^2}.$$

The self-consistent eigenstates can be found by solving $\partial_\rho E = \partial_\psi E = 0$, yielding the particle and condensate densities as

$$\rho = \frac{6t + \mu}{12t + 6(V + V')}, \tag{A2}$$

$$\psi = \frac{\sqrt{(6t + \mu)[6t + 6(V + V') - \mu]}}{12t + 6(V + V')}. \tag{A3}$$

Energies of the solid phases are obtained as expectation values of the full Bose-Hubbard Hamiltonian (5) in states with corresponding fillings $(\frac{1}{3}, \frac{2}{3}, 1)$ on the triangular unit cell. Normalizing energies and chemical potential by the scale $|V| + |V'|$, we may write the dimensionless per-site energies

of the solid and superfluid (SF) phases as

$$\tilde{E}_{j/3} = j\left[\frac{-\tilde{\mu}}{3} + \frac{\mathrm{sgn}(V)\,(j-1)/2 - 1}{\alpha+1}\right], \quad j = 1, 2, 3$$

$$\tilde{E}_{\mathrm{SF}} = -\frac{(6\tilde{t}+\tilde{\mu})^2(\alpha+1)}{24\tilde{t}(\alpha+1) + 12\,[\mathrm{sgn}(V)\alpha - 1]},$$

where we have introduced the notation $\tilde{c} \equiv c/(|V| + |V'|)$, and defined $\alpha \equiv |V/V'|$, with sgn(...) being the signum function.

To capture a possible supersolid phase (defined as one having simultaneously broken translational and gauge symmetries), we allow for more degrees of freedom in the mean-field decomposition. Considering the triangular unit cell with sites A, B, C, we assume

$$\psi_A \neq \psi_B = \psi_C \quad \text{and} \quad \rho_A \neq \rho_B = \rho_C.$$

Decoupling the mean-field Hamiltonian in Eq. (A1) for each unit cell yields

$$H_{\mathrm{MF},\triangle} = H_t + H_V + H_{V'} + H_\mu,$$

where

$$\begin{aligned}
H_t =& -3t\big[2\psi_B(b_A + b_A^\dagger) \\
&+ (\psi_A + \psi_B)(b_B + b_B^\dagger + b_C + b_C^\dagger) - 4\psi_A\psi_B - 2\psi_B^2\big], \\
H_V =& 3V\big[2\rho_B n_A + (\rho_A + \rho_B)(n_B + n_C) - 2\rho_A\rho_B - \rho_B^2\big], \\
H_{V'} =& 3V'\big[2\rho_A n_A + 2\rho_B(n_B + n_C) - \rho_A^2 - 2\rho_B^2\big], \\
H_\mu =& -\mu(n_A + n_B + n_C).
\end{aligned}$$

The energy E_{SS} of the resulting state can be found by numerical solution of

$$\partial_{\psi_A} E = \partial_{\psi_B} E = \partial_{\rho_A} E = \partial_{\rho_B} E = 0$$

at each point in $\tilde{\mu} - \tilde{t}$ phase space.

The values of V and V' to be used can be determined by Hartree-Fock calculations (see Appendix B) as a function of strain δ. Three distinct physical regimes arise in terms of their relative magnitudes, as discussed in Sec. III:

$$\begin{array}{ll}
|V| \gg |V'|,\ V > 0 & \text{unstrained} \\
|V| \simeq |V'|,\ V > 0 & \text{moderate strain} \\
|V| \simeq |V'|,\ V < 0 & \text{large strain.}
\end{array}$$

Thus, by changing the ratio $|V/V'|$, different mean-field phase diagrams can be generated, as shown in Fig. 3. To obtain a realistic phase diagram for the ^{4}He-on-graphene system over a range of physical parameters, one uses the Hartree-Fock results for $t(\delta)$, $V(\delta)$, and $V'(\delta)$ (see Fig. 4), which leads to the phase diagram in Fig. 8. The qualitative features of this mean-field phase diagram, including the existence of a superfluid strip and a $n = 1$ commensurate solid, are in qualitative agreement with Fig. 6 in the main text.

APPENDIX B: HARTREE-FOCK METHOD

Since many-body quantum Monte Carlo simulations are time consuming, we employed a computationally cheaper method, based on the Hartree-Fock (HF) approximation, to compute V and V' in Eq. (5) to be used in the strain-tuned mean-field phase diagram. The HF ansatz for the wave function Ψ for N bosons is

$$\Psi(\mathbf{r}_1, \mathbf{r}_2, \ldots, \mathbf{r}_N) = \sum_{j(q)} \prod_{q=1}^{N} \phi_{j(q)}(\mathbf{r}_q), \tag{B1}$$

where $\mathbf{r}_q$ are the three-dimensional (3D) coordinates of particle q, $j(q)$ is a label of the triangular site where particle q is found, and the one-particle quasi-wave functions (in what follows we will drop "quasi") satisfy the orthonormality conditions

$$\langle\phi_i|\phi_j\rangle \equiv \int d^2\mathbf{r}\,\phi_i^\dagger(\mathbf{r})\phi_j(\mathbf{r}) = \delta_{i,j}, \tag{B2}$$

with the † standing for Hermitian conjugation. Employing an approximation $\phi_i(\mathbf{r}) \approx \chi(z)\psi_i(\mathbf{r})$, where $\mathbf{r}$ is the 2D coordinate in the plane parallel to the graphene sheet and z is the perpendicular coordinate, the 2D-reduced wave function can be shown to satisfy HF equations

$$\begin{aligned}
&-\frac{\hbar^2}{2m}\nabla_{\mathbf{r}}^2\psi_i(\mathbf{r}) + \mathcal{V}_{\hexagon}(\mathbf{r})\psi_i(\mathbf{r}) \\
&\quad + \sum_{i\neq j}\int d\mathbf{r}'\,\psi_j^*(\mathbf{r}')\mathcal{V}(\mathbf{r}-\mathbf{r}')[\psi_j(\mathbf{r}')\psi_i(\mathbf{r}) + \psi_i(\mathbf{r}')\psi_j(\mathbf{r})] \\
&\quad = \sum_j E_{ij}\psi_j(\mathbf{r}),
\end{aligned} \tag{B3}$$

where the Lagrange multipliers E_{ij} are determined by the 2D form of the orthonormality conditions (B2). The 2D nature of the wave function is supported by quantum Monte Carlo calculations of the density profile in the z direction, as shown in Fig. 2. Additional details of the above approximations, as well as of the solution method of Eq. (B3), were outlined in [43]. In Eq. (B3), $\mathcal{V}_{\hexagon}(\mathbf{r})$ is computed as

$$\mathcal{V}_{\hexagon}(\mathbf{r}) \equiv \left\langle \frac{\int dz\,\mathcal{V}_{\hexagon}(\mathbf{r},z)\rho(\mathbf{r},z)}{\int dz\,\rho(\mathbf{r},z)} \right\rangle, \tag{B4}$$

where $\rho(\mathbf{r}, z)$ is the probability density obtained with one-particle (and hence relatively fast) quantum Monte Carlo simulations, and the angle brackets stand for the ensemble average. Furthermore, $\mathcal{V}(\mathbf{r})$ is the 2D reduction (as explained in Ref. [43]) of the interaction potential $\mathcal{V}(\mathbf{r}, z)$ between two helium atoms. In a slight deviation from [43], here for the computation of the reduced 2D potential, we used the one-dimensional probability density $\rho(z) \equiv \int d\mathbf{r}\,\rho(\mathbf{r}, z)$, with the $\rho(\mathbf{r}, z)$ as defined above. Then, parameter V in Eq. (5) is computed as

$$V = \iint d\mathbf{r}\,d\mathbf{r}'\,|\psi_i(\mathbf{r})|^2\mathcal{V}(\mathbf{r}-\mathbf{r}')|\psi_j(\mathbf{r}')|^2, \tag{B5}$$

where i and j are the indices of the two nearest-neighbor graphene cells. Parameter V' is defined similarly, but for the next-nearest neighbors. Finally, parameter t is computed as described in [43], using one-particle Wannier functions for a single helium atom over the graphene sheet.

APPENDIX C: QUANTUM MONTE CARLO

The strained graphene plus ^{4}He system described by the Hamiltonian in Eq. (1) was simulated using a stochastically

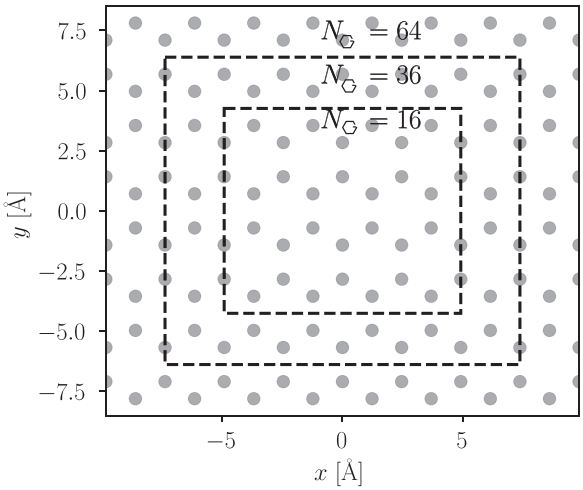

FIG. 9. Finite-size simulation cell. Three characteristic system sizes used for finite-size scaling, where periodic boundary conditions restrict the box dimensions to be a multiple of lattice vectors in the x and y directions. The resulting box size is a function of strain δ, and $N_\square$ refers to the number of triangular lattice adsorption sites in the simulation cell.

exact quantum Monte Carlo (QMC) algorithm exploiting path integrals [43,50,66]. Finite-temperature expectation values of observables $\mathcal{O}$ in the grand canonical ensemble were sampled via

$$\langle \mathcal{O} \rangle = \frac{1}{\mathcal{Z}} \mathrm{Tr}[\mathcal{O}\, \mathrm{e}^{-\beta(H-\mu N)}], \tag{C1}$$

where $\beta = 1/T$ is the inverse temperature ($k_\mathrm{B} = 1$), and the grand partition function $\mathcal{Z} = \mathrm{Tr}\mathrm{e}^{-\beta(H-\mu N)}$ can be written as a sum of discrete imaginary-time paths (world lines) over the set of all permutations $\mathcal{P}$ of the first-quantized labels of the N indistinguishable ^{4}He atoms. Algorithmic details have been reported elsewhere (e.g., Refs. [43,67,68]) and our QMC software is available online [51].

1. Simulation cell

The simulation cell is defined by a rectangular prism of dimensions $L_x \times L_y \times L_z$ where L_x and L_y are chosen such that the strained graphene sheet is compatible with periodic boundary conditions in the x and y directions. A membrane with $N_\square = 2N_xN_y$ triangular lattice adsorption sites requires that $L_x = a_0(1+\delta)\sqrt{3}N_x$ for the zigzag direction and $L_y = 3a_0(1+\delta)N_y$ for the armchair direction. Three of the box sizes corresponding to different numbers of adsorption sites used for finite-size scaling our QMC results to the thermodynamic limit are shown in Fig. 9.

2. Observables

To map out the phase diagram reported in Fig. 4 in the main text, we have computed a number of observables obtained via quantum Monte Carlo estimators. The total number of ^{4}He atoms in the simulation cell can fluctuate in the grand canonical ensemble at fixed temperature T and chemical potential μ leading to an average value $\langle N \rangle$ and filling fraction

$$n \equiv \frac{\langle N \rangle}{N_\square}, \tag{C2}$$

where $N_\square$ is set by the geometry of the simulation cell, and utilizing the fact that all atoms are adsorbed. The density of ^{4}He is given by

$$\rho(\boldsymbol{r}) = \left\langle \frac{1}{N} \sum_{i=1}^{N} \delta(\boldsymbol{r} - \boldsymbol{r}_i) \right\rangle, \tag{C3}$$

where $\delta(\dots)$ is the Dirac delta function. The planar density of ^{4}He adsorbed to the graphene can be computed by integrating over z: $\rho(x,y) = \int dz\, \rho(\boldsymbol{r})$ and its resulting compressibility is given by the usual fluctuation measure

$$\kappa = \frac{\langle N^2 \rangle - \langle N \rangle^2}{k_\mathrm{B} T L_x L_y}. \tag{C4}$$

Finally, the superfluid density ρ_s is related to the response of the free energy to a boundary phase twist [69] which can be captured in QMC via the topological winding number $\boldsymbol{W}$ of particle world lines around the simulation cell [54,70,71]:

$$\rho_s = \frac{m_4^2}{2\hbar^2 \beta L_x L_y} \left(L_x^2 \langle W_x^2 \rangle + L_y^2 \langle W_y \rangle^2 \right), \tag{C5}$$

where

$$W_x = \frac{1}{L_x} \sum_{i=1}^{N} \int_0^{\hbar\beta} \mathrm{d}\tau \left[\frac{\mathrm{d}x_i(\tau)}{\mathrm{d}\tau} \right]. \tag{C6}$$

with m_4 the mass of a ^{4}He atom and $x_i(\tau)$ the x coordinate of the imaginary-time world line corresponding to atom i.

3. Simulation details and finite-size scaling

Quantum Monte Carlo calculations were performed for $T = 0.5$–2.0 K and chemical potentials μ from -129–-41 K at system sizes corresponding to $N_\square = 16, 36, 64, 90, 144$ triangular lattice adsorption sites to obtain particle configurations at values of the isotropic strain $\delta = 0$ (unstrained) to $\delta = 0.3$ (strongly strained). The imaginary-time step was fixed at $\tau = 0.00313\,\mathrm{K}^{-1}$ such that any systematic effects due to Trotterization are smaller than statistical sampling errors. While quantum Monte Carlo simulations are performed at fixed system size (in the grand canonical ensemble), measurements of superfluid and particle densities were obtained via a finite-size scaling procedure at each temperature to extrapolate to the thermodynamic limit. Details are shown in Fig. 10, where we have assumed the finite-size scaling forms $n(N) = n|_\infty + O(1/N)$ and $\rho_s(N) = \rho_s|_\infty + O(1/\sqrt{N})$. The superfluid phase boundary in Fig. 6 was determined by performing this finite-size scaling procedure at 65 (δ, μ) points and identifying as superfluid any point where ρ_s persists in the thermodynamic limit for temperatures greater than $T = 0.5$ K (the base T in our quantum Monte Carlo study). Error bars on composite estimators (such as the compressibility) were estimated via jackknife sampling [72].

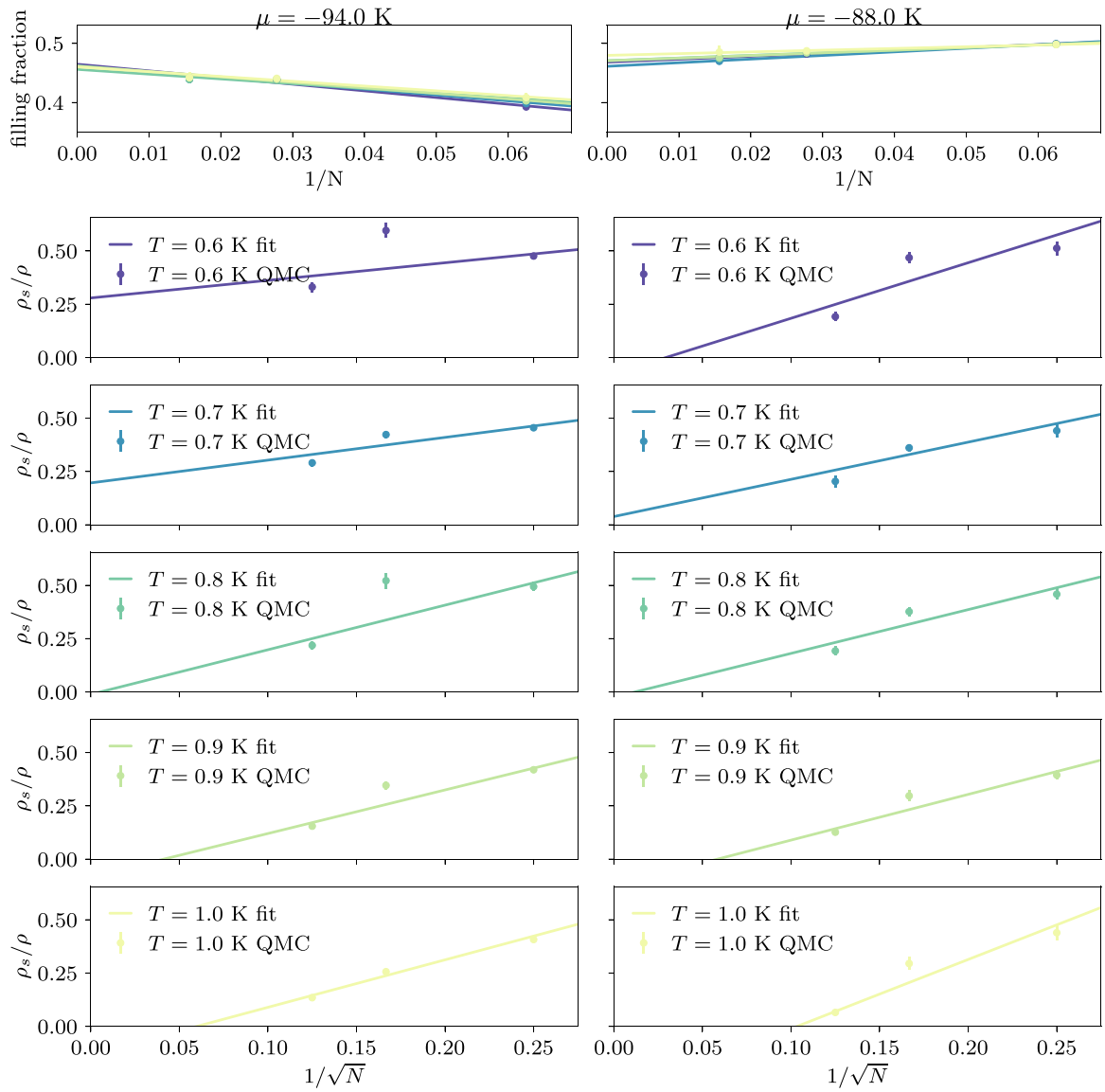

FIG. 10. Finite-size scaling of the particle and superfluid density. For each (δ, μ) data point, the existence of a superfluid phase in the thermodynamic limit is investigated by finite-size scaling of quantum Monte Carlo (QMC) data points. Columns show this procedure at two different values of μ for $\delta = 0.12$. For $\mu = -94.0\,\mathrm{K}$, superfluidity persists below $T = 0.7\,\mathrm{K}$, while no region of superfluidity is found for $\mu = -88\,\mathrm{K}$ in the thermodynamic limit. The form of the linear scaling functions (lines) for the filling fraction (top row) and superfluid fraction ρ_s/ρ (rows 2–6) is described in Appendix C 3. Error bars represent standard statistical uncertainties in quantum Monte Carlo.

[1] E. Altman, K. R. Brown, G. Carleo, L. D. Carr, E. Demler, C. Chin, B. DeMarco, S. E. Economou, M. A. Eriksson, K.-M. C. Fu, M. Greiner, K. R. A. Hazzard, R. G. Hulet, A. J. Kollár, B. L. Lev, M. D. Lukin, R. Ma, X. Mi, S. Misra, C. Monroe *et al.*, Quantum simulators: Architectures and opportunities, PRX Quantum **2**, 017003 (2021).

[2] I. Bloch, J. Dalibard, and W. Zwerger, Many-body physics with ultracold gases, Rev. Mod. Phys. **80**, 885 (2008).

[3] M. Lewenstein, A. Sanpera, V. Ahufinger, B. Damski, A. Sen(De), and U. Sen, Ultracold atomic gases in optical lattices: Mimicking condensed matter physics and beyond, Adv. Phys. **56**, 243 (2007).

[4] D.-W. Zhang, Y.-Q. Zhu, Y. X. Zhao, H. Yan, and S.-L. Zhu, Topological quantum matter with cold atoms, Adv. Phys. **67**, 253 (2018).

[5] A. H. Castro Neto, F. Guinea, N. M. R. Peres, K. S. Novoselov, and A. K. Geim, The electronic properties of graphene, Rev. Mod. Phys. **81**, 109 (2009).

[6] A. K. Geim and I. V. Grigorieva, Van der Waals heterostructures, Nature (London) **499**, 419 (2013).

[7] G. Semeghini, H. Levine, A. Keesling, S. Ebadi, T. T. Wang, D. Bluvstein, R. Verresen, H. Pichler, M. Kalinowski, R. Samajdar, A. Omran, S. Sachdev, A. Vishwanath, M. Greiner, V. Vuletić, and M. D. Lukin, Probing topological spin liquids

on a programmable quantum simulator, Science **374**, 1242 (2021).

[8] R. Ma, B. Saxberg, C. Owens, N. Leung, Y. Lu, J. Simon, and D. I. Schuster, A dissipatively stabilized Mott insulator of photons, Nature (London) **566**, 51 (2019).

[9] F. Ming, X. Wu, C. Chen, K. D. Wang, P. Mai, T. A. Maier, J. Strockoz, J. W. F. Venderbos, C. González, J. Ortega, S. Johnston, and H. H. Weitering, Evidence for chiral superconductivity on a silicon surface, Nat. Phys. **19**, 500 (2023).

[10] A. Kreisel, T. Hyart, and B. Rosenow, Tunable topological states hosted by unconventional superconductors with adatoms, Phys. Rev. Res. **3**, 033049 (2021).

[11] A. Del Maestro, C. Wexler, J. M. Vanegas, T. Lakoba, and V. N. Kotov, A perspective on collective properties of atoms on 2D materials, Adv. Electron. Mater. **8**, 2100607 (2022).

[12] R. P. Henkel, E. N. Smith, and J. D. Reppy, Temperature dependence of the superfluid healing length, Phys. Rev. Lett. **23**, 1276 (1969).

[13] J. M. Kosterlitz and D. J. Thouless, Ordering, metastability and phase transitions in two-dimensional systems, J. Phys. C: Solid State Phys. **6**, 1181 (1973).

[14] G. Agnolet, D. F. McQueeney, and J. D. Reppy, Kosterlitz-Thouless transition in helium films, Phys. Rev. B **39**, 8934 (1989).

[15] M. Bretz and J. G. Dash, Quasiclassical and quantum degenerate helium monolayers, Phys. Rev. Lett. **26**, 963 (1971).

[16] M. Bretz, J. G. Dash, D. C. Hickernell, E. O. McLean, and O. E. Vilches, Phases of He^3 and He^4 monolayer films adsorbed on basal-plane oriented graphite, Phys. Rev. A **8**, 1589 (1973).

[17] G. Zimmerli and M. H. W. Chan, Complete wetting of helium on graphite, Phys. Rev. B **38**, 8760 (1988).

[18] D. S. Greywall and P. A. Busch, Heat capacity of fluid monolayers of ^{4}He, Phys. Rev. Lett. **67**, 3535 (1991).

[19] G. Zimmerli, G. Mistura, and M. H. W. Chan, Third-sound study of a layered superfluid film, Phys. Rev. Lett. **68**, 60 (1992).

[20] P. A. Crowell and J. D. Reppy, Superfluidity and film structure in He^4 adsorbed on graphite, Phys. Rev. B **53**, 2701 (1996).

[21] J. Nyéki, R. Ray, B. Cowan, and J. Saunders, Superfluidity of atomically layered ^{4}He films, Phys. Rev. Lett. **81**, 152 (1998).

[22] P. A. Whitlock, G. V. Chester, and B. Krishnamachari, Monte Carlo simulation of a helium film on graphite, Phys. Rev. B **58**, 8704 (1998).

[23] P. Corboz, M. Boninsegni, L. Pollet, and M. Troyer, Phase diagram of ^{4}He adsorbed on graphite, Phys. Rev. B **78**, 245414 (2008).

[24] M. E. Pierce and E. Manousakis, Role of substrate corrugation in helium monolayer solidification, Phys. Rev. B **62**, 5228 (2000).

[25] J. Ahn, H. Lee, and Y. Kwon, Prediction of stable $C_{7/12}$ and metastable $C_{4/7}$ commensurate solid phases for ^{4}He on graphite, Phys. Rev. B **93**, 064511 (2016).

[26] M. Boninsegni and N. V. Prokof'ev, *Colloquium:* Supersolids: What and where are they?, Rev. Mod. Phys. **84**, 759 (2012).

[27] S. Wessel and M. Troyer, Supersolid hard-core bosons on the triangular lattice, Phys. Rev. Lett. **95**, 127205 (2005).

[28] S. Nakamura, K. Matsui, T. Matsui, and H. Fukuyama, Possible quantum liquid crystal phases of helium monolayers, Phys. Rev. B **94**, 180501(R) (2016).

[29] J. Nyéki, A. Phillis, A. Ho, D. Lee, P. Coleman, J. Parpia, B. Cowan, and J. Saunders, Intertwined superfluid and density wave order in two-dimensional ^{4}He, Nat. Phys. **13**, 455 (2017).

[30] J. Choi, A. A. Zadorozhko, J. Choi, and E. Kim, Spatially modulated superfluid state in two-dimensional ^{4}He films, Phys. Rev. Lett. **127**, 135301 (2021).

[31] M. C. Gordillo and J. Boronat, ^{4}He on a single graphene sheet, Phys. Rev. Lett. **102**, 085303 (2009).

[32] M. C. Gordillo, C. Cazorla, and J. Boronat, Supersolidity in quantum films adsorbed on graphene and graphite, Phys. Rev. B **83**, 121406(R) (2011).

[33] M. C. Gordillo and J. Boronat, Zero-temperature phase diagram of the second layer of ^{4}He adsorbed on graphene, Phys. Rev. B **85**, 195457 (2012).

[34] Y. Kwon and D. M. Ceperley, ^{4}He adsorption on a single graphene sheet: Path-integral Monte Carlo study, Phys. Rev. B **85**, 224501 (2012).

[35] J. Happacher, P. Corboz, M. Boninsegni, and L. Pollet, Phase diagram of ^{4}He on graphene, Phys. Rev. B **87**, 094514 (2013).

[36] M. C. Gordillo, Diffusion Monte Carlo calculation of the phase diagram of ^{4}He on corrugated graphene, Phys. Rev. B **89**, 155401 (2014).

[37] L. V. Markić, P. Stipanović, I. Bešlić, and R. E. Zillich, Solidification of ^{4}He clusters adsorbed on graphene, Phys. Rev. B **94**, 045428 (2016).

[38] M. Huang, H. Yan, C. Chen, D. Song, T. F. Heinz, and J. Hone, Phonon softening and crystallographic orientation of strained graphene studied by Raman spectroscopy, Proc. Natl. Acad. Sci. USA **106**, 7304 (2009).

[39] G. G. Naumis, S. Barraza-Lopez, M. Oliva-Leyva, and H. Terrones, Electronic and optical properties of strained graphene and other strained 2D materials: A review, Rep. Prog. Phys. **80**, 096501 (2017).

[40] J. Zabel, R. R. Nair, A. Ott, T. Georgiou, A. K. Geim, K. S. Novoselov, and C. Casiraghi, Raman spectroscopy of graphene and bilayer under biaxial strain: Bubbles and balloons, Nano Lett. **12**, 617 (2012).

[41] C. Androulidakis, E. N. Koukaras, J. Parthenios, G. Kalosakas, K. Papagelis, and C. Galiotis, Graphene flakes under controlled biaxial deformation, Sci. Rep. **5**, 18219 (2015).

[42] M. Przybytek, W. Cencek, J. Komasa, G. Łach, B. Jeziorski, and K. Szalewicz, Relativistic and quantum electrodynamics effects in the helium pair potential, Phys. Rev. Lett. **104**, 183003 (2010).

[43] J. Yu, E. Lauricella, M. Elsayed, K. Shepherd Jr., N. S. Nichols, T. Lombardi, S. W. Kim, C. Wexler, J. M. Vanegas, T. Lakoba, V. N. Kotov, and A. Del Maestro, Two-dimensional Bose-Hubbard model for helium on graphene, Phys. Rev. B **103**, 235414 (2021).

[44] W. Cencek, M. Przybytek, J. Komasa, J. B. Mehl, B. Jeziorski, and K. Szalewicz, Effects of adiabatic, relativistic, and quantum electrodynamics interactions on the pair potential and thermophysical properties of helium, J. Chem. Phys. **136**, 224303 (2012).

[45] W. A. Steele, The physical interaction of gases with crystalline solids: I. Gas-solid energies and properties of isolated adsorbed atoms, Surf. Sci. **36**, 317 (1973).

[46] N. S. Nichols, A. Del Maestro, C. Wexler, and V. N. Kotov, Adsorption by design: Tuning atom-graphene van der Waals

interactions via mechanical strain, Phys. Rev. B **93**, 205412 (2016).
[47] N. S. Nichols, 3D lookup tables for helium graphene interaction for isotropic strained graphene, version 1.1.0, Zenodo (2021), https://zenodo.org/doi/10.5281/zenodo.4990225.
[48] G. T. Zimanyi, P. A. Crowell, R. T. Scalettar, and G. G. Batrouni, Bose-Hubbard model and superfluid staircases in ^{4}He films, Phys. Rev. B **50**, 6515(R) (1994).
[49] G. Murthy, D. Arovas, and A. Auerbach, Superfluids and supersolids on frustrated two-dimensional lattices, Phys. Rev. B **55**, 3104 (1997).
[50] D. M. Ceperley, Path integrals in the theory of condensed helium, Rev. Mod. Phys. **67**, 279 (1995).
[51] A. Del Maestro, N. S. Nichols, M. Graves, and C. Herdman, Github Repository: Path Integral Quantum Monte Carlo https://github.com/DelMaestroGroup/pimc (2022), permanent link: https://doi.org/10.5281/zenodo.7271913
[52] A. Del Maestro and S. W. Kim, QMC Raw Data for Superfulid Helium Adsorbed on Strained Graphene, version 1.0.0, Zenodo (2022), https://doi.org/10.5281/zenodo.7271852.
[53] S. W. Kim and A. D. Maestro, Github repository: https://github.com/DelMaestroGroup/papers-code-Superfluid4HeStrainGraphene (2022), permanent link: https://doi.org/10.5281/zenodo.7294691.
[54] E. L. Pollock and D. M. Ceperley, Path-integral computation of superfluid densities, Phys. Rev. B **36**, 8343 (1987).
[55] C. Lee, X. Wei, J. W. Kysar, and J. Hone, Measurement of the elastic properties and intrinsic strength of monolayer graphene, Science **321**, 385 (2008).
[56] K. Cao, S. Feng, Y. Han, L. Gao, T. H. Ly, Z. Xu, and Y. Lu, Elastic straining of free-standing monolayer graphene, Nat. Commun. **11**, 284 (2020).
[57] T. M. G. Mohiuddin, A. Lombardo, R. R. Nair, A. Bonetti, G. Savini, R. Jalil, N. Bonini, D. M. Basko, C. Galiotis, N. Marzari, K. S. Novoselov, A. K. Geim, and A. C. Ferrari, Uniaxial strain in graphene by Raman spectroscopy: G peak splitting, Grüneisen parameters, and sample orientation, Phys. Rev. B **79**, 205433 (2009).
[58] F. Carrascoso, R. Frisenda, and A. Castellanos-Gomez, Biaxial versus uniaxial strain tuning of single-layer MoS_2, Nano Mater. Sci. **4**, 44 (2022).
[59] R. Roldán, A. Castellanos-Gomez, E. Cappelluti, and F. Guinea, Strain engineering in semiconducting two-dimensional crystals, J. Phys.: Condens. Matter **27**, 313201 (2015).
[60] B. Amorim, A. Cortijo, F. de Juan, A. G. Grushin, F. Guinea, A. Gutiérrez-Rubio, H. Ochoa, V. Parente, R. Roldán, P. San-Jose, J. Schiefele, M. Sturla, and M. A. H. Vozmediano, Novel effects of strains in graphene and other two dimensional materials, Phys. Rep. **617**, 1 (2016).
[61] J. C. Meyer, A. K. Geim, M. I. Katsnelson, K. S. Novoselov, T. J. Booth, and S. Roth, The structure of suspended graphene sheets, Nature (London) **446**, 60 (2007).
[62] J. Manninen, A. Laitinen, F. Massel, and P. Hakonen, Mechanical Detection of the De Haas–van Alphen effect in graphene, Nano Lett. **22**, 9869 (2022).
[63] A. Yamaguchi, H. Tajiri, A. Kumashita, J. Usami, Y. Yamane, A. Sumiyama, M. Suzuki, T. Minoguchi, Y. Sakurai, and H. Fukuyama, Structural study of adsorbed helium films: New approach with synchrotron radiation X-rays, J. Low Temp. Phys. **208**, 441 (2022).
[64] J. Usami, R. Toda, S. Nakamura, T. Matsui, and H. Fukuyama, A simple experimental setup for simultaneous superfluid-response and heat-capacity measurements for helium in confined geometries, J. Low Temp. Phys. **208**, 457 (2022).
[65] I. Todoshchenko, M. Kamada, J.-P. Kaikkonen, Y. Liao, A. Savin, M. Will, E. Sergeicheva, T. S. Abhilash, E. Kauppinen, and P. J. Hakonen, Topologically-imposed vacancies and mobile solid ^{3}He on carbon nanotube, Nat. Commun. **13**, 5873 (2022).
[66] M. Boninsegni, N. Prokof'ev, and B. Svistunov, Worm algorithm for continuous-space path integral Monte Carlo simulations, Phys. Rev. Lett. **96**, 070601 (2006).
[67] N. S. Nichols, T. R. Prisk, G. Warren, P. Sokol, and A. Del Maestro, Dimensional reduction of helium-4 inside argon-plated MCM-41 nanopores, Phys. Rev. B **102**, 144505 (2020).
[68] A. Del Maestro, N. S. Nichols, T. R. Prisk, G. Warren, and P. E. Sokol, Experimental realization of one dimensional helium, Nat. Commun. **13**, 3168 (2022).
[69] M. E. Fisher, M. N. Barber, and D. Jasnow, Helicity modulus, superfluidity, and scaling in isotropic systems, Phys. Rev. A **8**, 1111 (1973).
[70] N. V. Prokof'ev and B. V. Svistunov, Two definitions of superfluid density, Phys. Rev. B **61**, 11282 (2000).
[71] V. G. Rousseau, Superfluid density in continuous and discrete spaces: Avoiding misconceptions, Phys. Rev. B **90**, 134503 (2014).
[72] P. Young, Everything you wanted to know about data analysis and fitting but were afraid to ask, arXiv:1210.3781.

Correction: Affiliation number 2 contained an error and has been fixed. An omission in the Acknowledgment section has been rectified.